ARTICLE

Enhanced electrocatalytic oxygen reduction reaction for Fe-N_4-C by incorporation of Co nanoparticles

Received 00th January 20xx,
Accepted 00th January 20xx

DOI: 10.1039/x0xx00000x

Tao Jiang,[a] Weiling Luan,*[a] Lyudmila Turyanska [b] and Qi Feng [c]

Oxygen reduction reaction (ORR) catalytic activity can be improved by means of enhancing the synergy between transition metals. In this work, novel porous Fe-N_4-C nanostructure enwrapping uniformly dispersed Co nanoparticle (CoNP) is prepared by an assisted thermal loading method. The as-prepared Co@Fe-N-C catalyst demonstrates enhanced ORR activity with a half-wave potential ($E_{1/2}$) of 0.92 V vs. RHE, which is much higher than the direct pyrolysis CoNPs-free sample Fe-N-C ($E_{1/2}$=0.85 V) and Pt/C ($E_{1/2}$=0.90 V) in alkaline media. It exhibits a remarkable stability with only 10 mV decrease in $E_{1/2}$ after 10,000 cycles and an outstanding long-term durability with current remains 85% after 60,000s. In acidic media, this catalyst exhibits catalytic activity with an $E_{1/2}$ of 0.79 V, comparable to Pt/C ($E_{1/2}$=0.82 V). The X-ray absorption fine spectroscopy analysis revealed presence of active centres of Fe-N_4. Density functional theory calculations confirmed the strong synergy between CoNPs and Fe-N_4 sites, providing a lower overpotential and beneficial electronic structure and local coordination environment for ORR. The incorporation of CoNPs on the surface of Fe-N_4-C nanomaterials plays a key role in enhancing the ORR catalytic activity and stability, providing a new route to prepare efficient Pt-free ORR catalysts.

Introduction

The exploration of precious metal-free catalysts for the oxygen reduction reaction (ORR) is a major concern to achieve the practical application of fuel cells and metal–air batteries.[1,2] Until now, materials based on noble metals, such as platinum (Pt)-, palladium (Pd)-, ruthenium (Ru)- and iridium (Ir)-based materials and their alloys, have been observed to exhibit optimal performance during this catalytic process.[3–5] However, certain precious metal-free catalysts with a comparable performance have rarely been reported.[6] Good catalytic activity has been achieved with respect to the ORR using transition metal nitrides,[7,8] carbides[9,10] and oxides,[11,12] particularly those based on transition metal and nitrogen co-doped carbon nanostructures (M-N-C, M = Fe, Co, Mn, Cr, Ni, etc).[13–17] Among these, Fe-N-C and Co-N-C materials are the most plausible alternatives to precious metal catalysts.[7,18] In particular, the Fe-N-C catalysts demonstrate prominent ORR catalytic performance that is comparable to that of Pt-based catalysts because of their efficient Fe-Nx active sites.[8,19] In addition, Fe carbide (Fe_3C) and Fe oxide (Fe_3O_4) play significant roles during the enhancement of the ORR catalytic activity.[20–22] The Co-N-C catalysts also exhibit excellent ORR catalytic ability because of their efficient Co-N_x active sites.[23] Importantly, in an acidic environment, the Co-N_x sites generally show higher stability than the Fe-N_x sites despite the superior catalytic activity of the latter.[24,25] Therefore, the development of high-performance and high-stability Co-based catalysts is attracting considerable attention. Generally, the preparation of non-precious metal-based catalysts requires high-temperature treatments. Unfortunately, at a high temperature, Co easily undergoes aggregation into nonuniform clusters at high temperatures, resulting in the insufficient exposure of the metal active sites and the concomitant reduction of the catalytic performance of the Co-based catalysts.[26]

Generally, a high catalytic performance is associated with a high specific surface area, high porosity, multidimensional pore distribution, high nitrogen content, and high graphitization degree.[27,28] Metal-organic frameworks (MOFs) have been extensively used as precursors to prepare ORR catalysts because of various crucial advantages such as large specific surface area, high porosity, and uniform metal and nitrogen distribution without external carbon supports, which are beneficial in case of ORR.[29,30] The zeolite imidazole frameworks (ZIFs) having cobalt (ZIF-67) or zinc (ZIF-8) as metal centers and dimethylimidazole as the ligands are the most commonly used precursors.[31] For example, ZIF-67 can generate Co-Nx active sites[32] and nitrogen-doped porous carbon nanostructures with a high degree of graphitization have been obtained from the pyrolysis of ZIF-8.[33] ZIF-8 can be easily doped using metal heteroatoms to prepare M-N_x active sites, and Zn atoms can be removed at a high temperature of >900 °C, resulting in abundant micropores beneficial for the ORR catalytic performance.[34] For instance, using the double-solvent method, Fe ions can be doped into the pores of ZIF-8; subsequently, Fe-Nx active sites can be generated after pyrolysis.[35–38] In addition, bimetal-based MOFs, such as Zn@Co-

[a] School of Mechanical and Power Engineering, East China University of Science and Technology, Shanghai 200237, China. E-mail: luan@ecust.edu.cn
[b] Faculty of Engineering, University of Nottingham, University Park, NG72RD, UK.
[c] Prospective Technology Department, SAIC Motorcycle Company, Shanghai 201800, China.

†Electronic Supplementary Information (ESI) available: Compositional and morphological characterization including SEM, XRD, BET, ICP, XPS, XAS of Co@Fe-N-C and references; Assessment of catalytic activity including LSV, Tafel, TEM images after long-term durability tests and ORR performance compared with other literature for Co@Fe-N-C and references; Acidic stability test of Co@Fe-N-C; DFT calculation including structure charts, free energy diagram, Fermi energy diagram of Co@Fe-N-C and Fe-N-C; Effect of growth conditions on CoNPs formation and catalytic activity including TEM, Photographs, Raman and LSV curves of Co@Fe-N-C treated with different temperature, Ar flow speeds, Fe and Co contents. See DOI: 10.1039/x0xx00000x

ZIF, have been proposed to produce highly porous catalysts with several Co-N_x active sites and exhibit high porosity and graphitization degree.[39] The Fe-doped bimetal catalyst showed excellent catalytic activity and stability.[40]

The catalytic activity of ORR can be enhanced based on the synergistic effect between transition metals, especially between Fe and Co.[41,42] The direct heat treatment of Co-ZIF at high temperature leads to formation of Co-N_x sites. Also, carbonization of ZIFs can result in partial release of Co^{2+} ions and formation of Co nanoparticles (CoNPs) during sintering.[43] Thus, CoNPs are expected to uniformly disperse on the surface of Fe-N-C catalyst, hindering the undesirable agglomeration of Co and enhancing the synergy between Co and Fe. Herein, we report a novel Co@Fe-N-C catalyst produced by an assisted thermal loading method based on Co-ZIF and Fe-ZIF, and containing CoNPs uniformly loaded on the surface of Fe-N_4-C nanomaterials. The Co@Fe-N-C catalyst demonstrates enhanced ORR catalytic activity in alkaline media (0.1 M KOH, $E_{1/2}$ of 0.92 V vs. RHE). The enhancement of the catalytic performance is correlated with the density and distribution of CoNPs and their interaction with Fe-sites. The observed performance is greater than that of Fe-N-C with no CoNPs, Co@N-C without Fe doping, N-C without metal doping, commercial Pt/C catalyst, and most of other reported Fe- and Fe-Co bimetal-based catalysts. In addition, the Co@Fe-N-C catalyst has outstanding activity in more challenging acidic environment (0.1 M $HClO_4$) with $E_{1/2}$ of 0.79 V that is comparable to commercial Pt/C catalyst. The active centres and origin of the enhanced ORR catalytic performance is discussed based on X-ray absorption fine spectroscopy analysis and density functional theory (DFT) calculations.

Experimental

Chemicals

All the reactants were purchased as stated below and used without any purification. Zinc nitrate hexahydrate ($Zn(NO_3)_2{\cdot}6H_2O$), cobalt nitrate hexahydrate ($Co(NO_3)_2{\cdot}6H_2O$), ferric chloride hexahydrate ($FeCl_3{\cdot}6H_2O$), dimethylimidazole (2-MeIM), potassium hydroxide (KOH), methanol (CH_3OH), and ethanol (C_2H_5OH) were purchased from Titan (Shanghai, China). Then, sulfuric acid is purchased from Alfa, and Nafion (5%) was purchased from DuPont. Pt/C catalyst was purchased from Hesen (Shanghai, China). Ultrapure water with a resistivity of 18.2 MΩ was used during the process.

Synthesis of ZIFs

ZIF-8 was synthesized in accordance with a modified procedure reported in the literature.[14] Briefly, 40 mL of a CH_3OH solution containing 3.0 g (10 mmol) of $Zn(NO_3)_2{\cdot}6H_2O$ was added to 80 mL of a CH_3OH solution containing 6.5 g (80 mmol) of 2-MeIM, and the resulting mixture was stirred for 24 h at room temperature, followed by centrifugal washing (5 min at 5000 rpm) that was repeated thrice with CH_3OH and overnight drying in vacuum at 70 °C. The resulting white powder was collected and stored at room temperature. Co-ZIF was synthesized via the same method using a CH_3OH solution (500 mL) containing 12.3 g (150 mmol) of 2-MeIM and a solution of MeOH (500 mL) containing 7.3 g (25 mmol) of $Co(NO_3)_2{\cdot}6H_2O$; finally, the obtained purple powder was collected.

Synthesis of Fe-ZIF-8

First, ZIF-8 (100 mg) was dispersed in MeOH (15 mL) and ultrasonicated for 15 min. This was followed by the injection of 150 µL of an aqueous solution of $FeCl_3{\cdot}6H_2O$ (50 mg mL^{-1}). Then, this mixture was ultrasonicated for 2 h and stirred for 1 h at room temperature. The light-yellow powder Fe-ZIF-8 powder was then collected after performing centrifugal cleaning twice using CH_3OH and overnight vacuum drying at 60 °C.

Preparation of catalysts

Co@Fe-N-C was prepared using an assisted thermal loading method. The corundum boat containing powder of Fe-ZIF-8 (100 mg) was placed next to corundum boat containing Co-ZIF (200 mg) in a quartz tube and were pyrolyzed in an inert gas atmosphere (see Fig. S1 in the ESI). The pyrolysis was performed at T = 900 °C with a heating rate of 5 °C min^{-1} for 2 h in Ar atmosphere, followed by cooling to room temperature. After being washed with 0.5 M H_2SO_4 for three times at room temperature to remove the inactive species and dried in vacuum oven, the black Co@Fe-N-C powder was collected and stored at room temperature. In order to assess the effect of CoNPs on the ORR activity, the Fe-N-C catalyst was prepared by direct pyrolysis of Fe-ZIF-8. The assisted thermal loading of ZIF-8 and Co-ZIF was used to prepare the Co@N-C and the direct pyrolysis of ZIF-8 was used to prepare the N-C (see Table S1 in the ESI).

Characterization

The sample morphology was investigated using scanning electron microscopy (SEM, Hitachi Limited S-4800), transmission electron microscopy (TEM, JEOL JEM-2100F), high-angle annular dark-field scanning transmission electron microscopy (HAADF-STEM, Hitachi S-5500), and aberration-corrected transmission electron microscopy (ACTEM, FEI Titan Themis TEM) were used to investigate the morphology of the samples. The crystal structure of the samples was analyzed using powder X-ray diffraction (XRD, Rigaku 2550VB). Raman spectra were recorded on an Invia/Reflrx Laser spectrometer (Renishaw, England) using a 532-nm laser beam for excitation. Further, inductively coupled plasma mass spectrometry (ICP MS, Baird PS-6) was used to measure the metal element content in the samples. The nitrogen adsorption and desorption method (Mike ASAP 2020 HD88) was used to estimate the specific surface area and obtain the pore size distribution. X-ray photoelectron spectroscopy (XPS) with an Al Kα X-ray source (Thermo ESCALAB250) was used for determining the chemical state and valence of the samples. X-ray absorption fine spectroscopy (XAFS) was used to investigate the fine chemical environment of the samples. An extended X-ray absorption fine structure (EXAFS) analysis was conducted on the X-ray Absorption Fine structure for catalysis (XAFCA) beamline at the Catalysis and Surface Science Endstation at Singapore Synchrotron

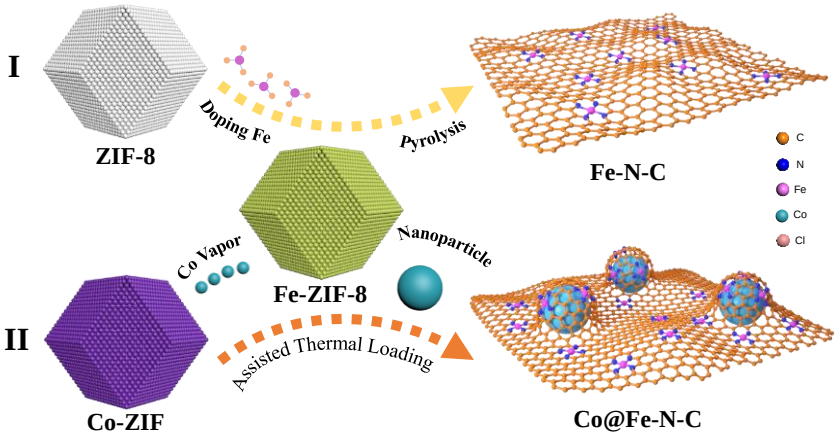

Figure 1. Schematic illustration for the synthesis of (I) Fe-N-C and (II) Co@Fe-N-C. Fe-ZIF-8 was prepared by adsorbing $FeCl_3$ molecules into the microporous of ZIF-8; Co nanoparticles loaded on the surface of Fe, N co-doped graphitic carbon nanomaterials during the process of calcination.

Light Source (SSLS). The EXAFS spectra were recorded using the Gaussian window function. The Fe K-edge X-ray near edge structure (XANES) data were recorded in the fluorescence mode. The detector was an ion chamber with a double-crystal Si (111) monochromator. The storage ring was operating at an energy of 700 MeV with an average electron current of 200 mA. The DFT calculation was used for calculating the free energy associated with the ORR of the catalysts (SI3, in the ESI).

Electrochemical performance tests

The electrochemical performance of the catalysts was evaluated using a three-electrode system comprising a rotating disk electrode (RDE, 5 mm in diameter) or rotating ring-disk electrode (RRDE, 4 mm in diameter for the disk and 5 mm in diameter for the ring) as the working electrode, Ag/AgCl (over saturated KCl) as the reference electrode, and graphite rod as the counter electrode. In this work, the potential values were calculated as formula: E (vs. RHE) = E (vs. Ag/AgCl) +0. 97 V. Subsequently, catalytic inks were prepared by dispersing 5 mg of the as-prepared catalysts in 470 µL of ethanol, 470 µL of ultrapure water, and 60 µL of Nafion or 5 mg of Pt/C in 960 µL of isopropanol and 40 µL of Nafion. The inks were ultrasonicated for 1 h. Then 5 µL of the ink was dropped on the RRDE as an alkaline work electrode (loading of 0.2 mg cm^{-2}) or 16 µL of the ink was dropped on the RDE as an acidic work electrode (loading of 0.4 mg cm^{-2}). The deposited inks were dried at room temperature. All the tests were conducted in O_2-saturated electrolyte solutions. In an alkaline electrolyte comprising the KOH solution (0.1 M), cyclic voltammetry (CV) curves could be observed from −1 to 0.2 V at a sweep rate of 50 mV s^{-1}. Linear sweep voltammetry (LSV) curves were recorded on the RRDE (rotating rates of 1600 rpm) from 0.2 to −1 V at a sweep rate of 10 mV s^{-1}. In an acidic electrolyte comprising an $HClO_4$ solution (0.1 M), CV curves were recorded in the range from −0.2 to 1 V and LSV curves were obtained on the RDE from 1 to −0.2 V. For the CV cycles stability test, the potential range was set from 0.6 to 1.0 V with a sweep rate of 100 mV s^{-1}. The electron transfer number, n, was calculated using the Koutecky-Levich equations in the ESI. The value of n and the yield of H_2O_2 can be calculated according to RRDE results and reference formula in the ESI. The collection efficiency (0.39) of the ring electrode measured in 1 M potassium ferricyanide ($K_3Fe(CN)_6$) and 0.1 M KCl solution. Note that the ring electrode potential was set at 1.48 V (vs. RHE).

Results and discussion

Synthesis and microscopic characterization of catalysts

ZIF-8 was doped with $FeCl_3$ and directly pyrolyzed to prepare Fe-N-C catalyst counterpart, as shown in process I of Fig. 1. The assisted thermal loading method was used to prepare the Co@Fe-N-C catalyst. As shown in process II of Fig. 1 and Fig. S1 in the ESI, Fe-ZIF-8 and Co-ZIF were placed in separate corundum boats and placed close to each other in the central position of a quartz tube, with the boat containing Co-ZIF located toward the inert gas inlet. After the pyrolysis process and washed with acid, Co@Fe-N-C was collected without any other post-processing. The SEM images and powder XRD patterns confirm the typical dodecahedral morphology of ZIF-8 (Fig. S2a, S3a in the ESI). Fe-ZIF-8 was formed by mixing the Fe^{3+} solution with ZIF-8 and it inherited the ZIF-8 structure. Fe^{3+} was embedded in the micropores of ZIF-8, which could be observed from the Brunauer-Emmett-Tellet (BET) and Barrett-Joyner-Halenda (BJH) results that denoted a smaller micropore volume in Fe-ZIF-8 when compared with that in ZIF-8 (Fig. S4 in the ESI). In contrast, the TEM image of Co@Fe-N-C (Fig. 2a) reveals many nanoparticles wrapped by graphitic-like carbons. The high-resolution TEM (HRTEM) image shows that the lattice spacing in these particles is 2.16 Å (Fig. 2b), which corresponds to the Co (100) plane. The CoNPs were also detected based on the HAADF-STEM and SEM results (Fig. 2c, Fig. S2c in the ESI), which revealed the presence of particles with average sizes of 20 ± 10 nm. The carbonization of Co-ZIF during heat

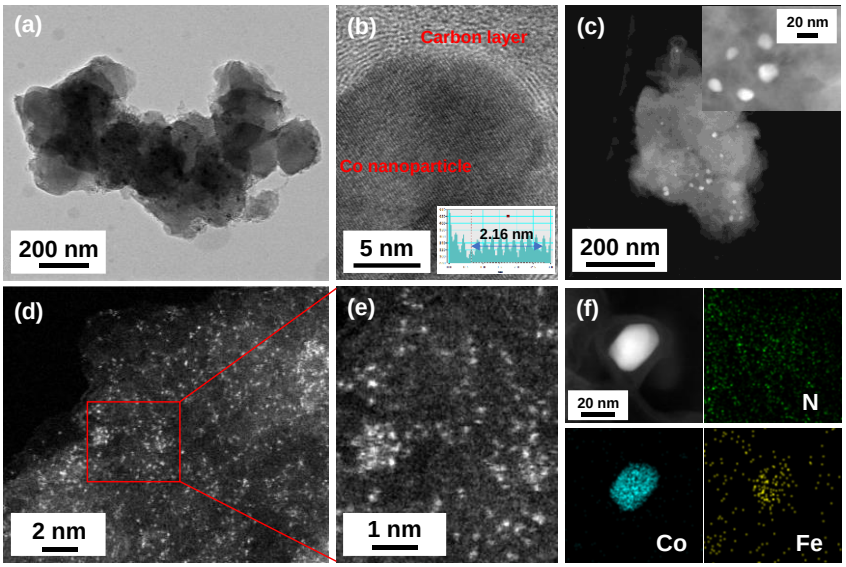

Figure 2. Micromorphology of Co@Fe-N-C. (a) TEM, (b) HRTEM, (c) HADDF-STEM of Co@Fe-N-C. (d, e) ACTEM of Co@Fe-N-C, showing atomic level distribution of Fe and several sub-nanoclusters. (f) High resolution HADDF-STEM image and corresponding elemental mapping of Co@Fe-N-C.

treatment results in release of Co^{2+} ions, some of which can be reduced to form CoNPs during sintering process.[12] We envisage that assisted thermal loading method, where the Fe-ZIF-8 is placed close to Co-ZIF which towards the outlet of the quartz tube in the tubular furnace, a small amount of Co is transferred with argon flow during carbonization process and the CoNPs are formed and embedded into the Fe-N_4-C. Thus, metallic CoNPs were thermally loaded on the surface of Fe-N-C nanomaterials after calcination. The SEM and TEM images of the Fe-N-C sample reveal a morphology comparable to that of Co@Fe-N-C; however, no CoNPs are observed (Fig. S5a, Fig. S6a, Fig. S6d in the ESI). It is also noted that no CoNPs are observed in any of our control samples (Fig. S6 in the ESI), indicating that the CoNPs might be formed because of the synergistic action between Fe and Co during the heating process. The existence of CoNPs is expected to enhance the synergy between CoNP and Fe species thus improves the ORR activity of Fe-N-C nanomaterials.

The metal distribution during catalysis is a major factor associated with its activity; therefore, the distribution of Fe in Co@Fe-N-C was assessed via ACTEM analysis (Fig. 2d, e). Fe is found to be distributed at the atomic level throughout the catalyst. Fig. 2f shows the high-resolution HAADF-STEM image and the corresponding elemental mapping, confirming the uniform distribution of N and Fe on the carbon matrix. In addition, Co could only be detected in the form of nanoparticles. The XRD patterns for Co@Fe-N-C and the reference samples reveal two peaks at 24° and 43° (Fig. S3b in the ESI), corresponding to the graphitic C (110) and C (200) planes, respectively. The Fe and metallic Co signals were not detected by XRD, probably due to that Fe are atomic level distribution as Fe-N_x and the small amount of CoNPs were wrapped in the graphitic nanocarbon materials. ICP results indicate Fe content is 12 times of Co content (Table S2 in the ESI). It is note-worthy that the surface roughness of Co@N-C sample is greater than that of the N-C sample (Fig. S6b, c in the ESI), which can be attributed to the increased degree of graphitization. This result was further confirmed by Raman spectroscopy analysis (Fig. 3a), which revealed a higher I_G/I_D value for Co@N-C (1.06) when compared with that for the N-C sample (0.92). The degrees of graphitization of the Fe-N-C sample and Co@N-C are identical (1.05) probably because of the similar catalytic effect of Fe and Co at high temperature. Importantly, Co@Fe-N-C demonstrates the highest I_G/I_D value (1.16), i.e., the highest degree of graphitization, which is beneficial for the ORR catalytic activity.

The N_2 adsorption and desorption curves (Fig. 3b) reveal that the BET specific surface area of Co@Fe-N-C is 1153 $m^2\ g^{-1}$, which is significantly greater than those of Fe-N-C (870 $m^2\ g^{-1}$) and N-C (887 $m^2\ g^{-1}$). The larger specific surface area corresponds to better ORR activity of M-N-C catalysts.[37] The corresponding pore size distribution shows the presence of micropores with two sizes (~0.7 nm and ~1.2 nm) in Co@Fe-N-C, whereas only micropores with a size of ~1.2 nm could be observed in the remaining two samples (Fig. 3c). The Co@Fe-N-C also has higher pore volume of 0.75 mL g^{-1} compared to Fe-N-C (0.56 mL g^{-1}) and N-C (0.62 mL g^{-1}), which is beneficial for the ORR activity of M-N-C catalysts. The observed high specific surface area is consistent with the smaller micropore size and large pore volume in Co@Fe-N-C. In addition, the highest BET specific surface area of 1352 $m^2\ g^{-1}$ is observed in Co@N-C. This could be attributed to the presence of a great number of micropores and mesopores due to the catalytic effect of Co-ZIF on ZIF-8 and the large pore volume (0.91 mL g^{-1}). Furthermore, only the Co@Fe-N-C and Co@N-C samples show hysteresis loops in N_2 adsorption and desorption curves, confirming the presence of mesopores, which is consistent with the pore size distribution result that indicates a size of 3.8 nm for Co@Fe-N-C and smaller sizes of 2.4 and 3.2 nm for Co@N-C.

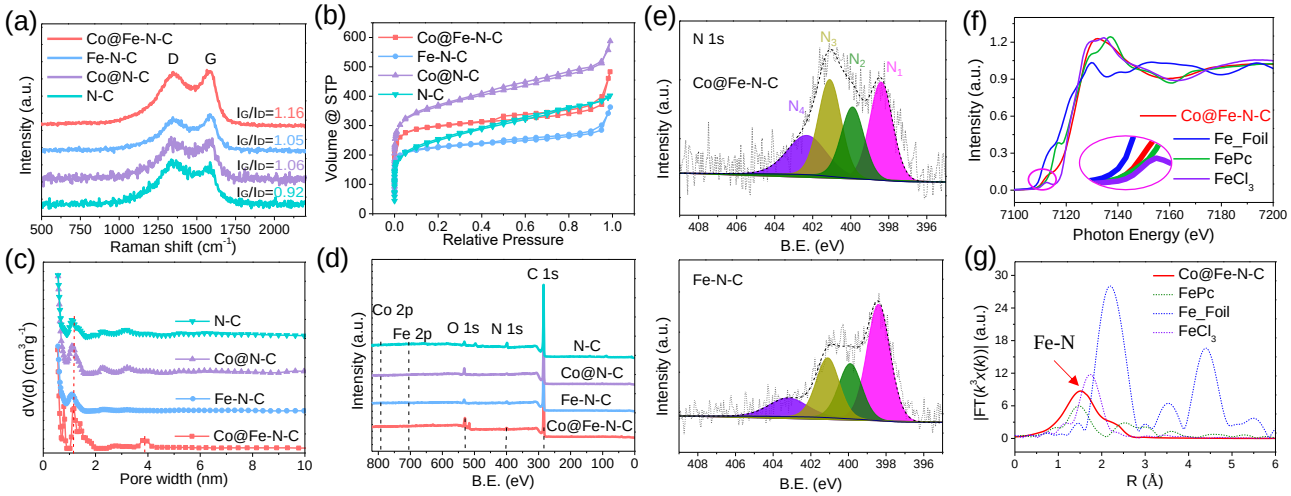

Figure 3. (a) Raman curves, (b) N_2 adsorption and desorption curves and (c) corresponding pore size of Co@Fe-N-C, Fe-N-C, Co@N-C and N-C. (d) XPS spectrums and (e) corresponding high-resolution XPS N 1s spectrums of Co@Fe-N-C, Fe-N-C, Co@N-C and N-C. (f) XANES and (g) FT-EXAFS curves of Co@Fe-N-C and references at Fe k-edge.

Chemical structure and coordination analysis

The chemical composition of the samples was investigated via XPS (Fig. 3d). The chemical state of N, e.g., pyridinic-N and graphitic-N, significantly affects the catalytic performance during the ORR.[44,45] The high-resolution XPS N 1s spectra (Fig. 3e) reveals four peaks at 398.4, 399.9, 401.1, and 402.3 eV, corresponding to pyridinic-N, Fe-N_x, graphitic-N, and oxidized-N,[46] respectively. Co@Fe-N-C exhibits similar Fe-N_x content (21.32%), when compared with those of Fe-N-C (21.06%). Importantly, an increase of the graphitic-N content is observed in Co@Fe-N-C (28.91%) compared to Fe-N-C (22.81%) which is beneficial for the ORR activity and the stability of M-N-C catalysts.[26] N 1s spectra of Co@N-C and N-C are shown in Fig. S7a in the ESI. The C 1s spectra of the samples are also analyzed and fitted to three peaks at 284.6, 286.2, and 288.2 eV, which correspond to C-C, C=N, and O-C=O,[47] respectively (Fig. S7b in the ESI). The chemical states of Fe and Co are not analyzed because of the low signal-to-noise ratio in the Fe 2p spectra and the Co 2p spectra. (Fig. S7c in the ESI).

As the metallic Co content of Co@Fe-N-C is too low to be detected by XAFS. Here, XAFS spectroscopy was used for examining the chemical environment of Fe in the Co@Fe-N-C catalyst. As shown in Fig. 3f, the XANES spectrum denotes that the pre-edge position of Co@Fe-N-C is between that of Fe foil and Fe(II) phthalocyanine (FePc) and is far left when compared with the position of $FeCl_3$. Thus, the valence state of Fe is between 0 and +2. The Fourier-transformed (FT) k3-weighted EXAFS spectra of Co@Fe-N-C and its references (Fig. 3g) reveal a dominant peak at ~1.5 Å, which could be attributed to the observed Fe-N bonds.[15,48] These results are consistent with the ACTEM and elemental mapping results, confirming the atomic-level distribution of Fe in Co@Fe-N-C. The EXAFS fitting results denote that the coordination number of Fe to N atoms is 3.7 ± 0.6, suggesting the presence of Fe-N_4 complexes in Co@Fe-N-C (Fig. S8 and Table S3 in the ESI). As we know, the ORR activity can be enhanced by the presence of efficient Fe-N_4 active centers.[49,50]

Electrochemical performances tests

The electrochemical performance of the samples was evaluated using a three-electrode system. The CV curves indicate peak potentials of 0.90 V vs. RHE for Co@Fe-N-C, 0.91 V for Pt/C, 0.84 V for Fe-N-C, 0.76 V for Co@N-C, and 0.72 V for N-C in O_2-saturated 0.1 M KOH solution (Fig. 4a). LSV curves are shown in Fig. 4b (vs. RHE electrode) and Fig. S9 in the ESI (vs. Ag/AgCl electrode). The onset potential is 1.03 V for Co@Fe-N-C, 1.02 V for Pt/C, 0.96 V for Fe-N-C, 0.88 V for Co@N-C, and 0.86 V for N-C. We observe higher $E_{1/2}$ for Co@Fe-N-C than CoNPs-free Fe-N-C, hence confirming beneficial effect of CoNPs in enhancing ORR activity (Fig. 4c). To confirm the effect of CoNPs and to distinguish between the effect of CoNPs and that or specific surface area and number of active sites, we examined ORR activity of catalyst with CoNP and after removal of CoNP by etching (0.5 M H2SO4 at 80 °C). The successful removal of CoNPs by etching was confirmed by TEM studies, which revealed presence of pores in place of the CoNPs (Fig. S10 in the ESI). The activity of etched Co@Fe-N-C-A was significantly reduced confirming the important role of CoNPs in ORR activity of Co@Fe-N-C. (Fig. S11a in the ESI). We summarise the ORR performance parameters for the Co@Fe-N-C, Co@Fe-N-C-A and Fe-N-C in Table S4 in the ESI. Furthermore, the RRDE results demonstrates that Co@Fe-N-C possesses the lowest ring current which is beneficial for the four-electron pathway in ORR (ring current in LSV curves, Fig. 4b). The catalytic activity of both Fe-containing catalysts, Co@Fe-N-C and Fe-N-C, was found to be higher than that of N-C, which confirms the important role of the Fe-N_4 sites as active centers. This Co@Fe-N-C catalyst also demonstrates comparable or higher ORR catalytic activity than most of the

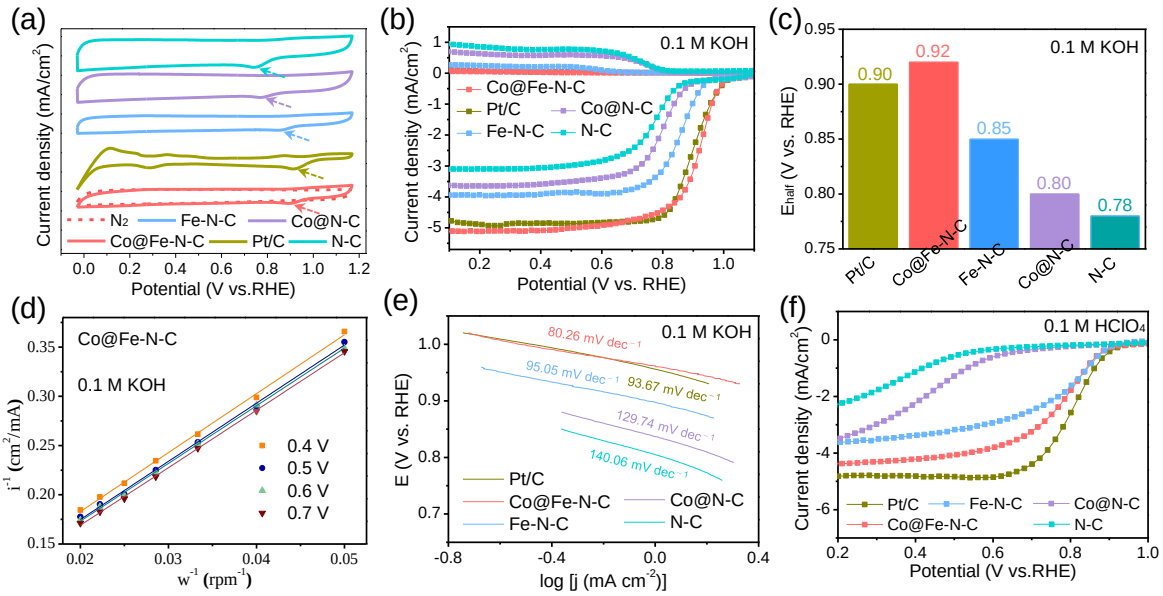

Figure 4. Electrocatalytic activity tests. (a) CV curves, (b) RRDE LSV curves, (c) half-wave potential of Pt/C, Co@Fe-N-C, Fe-N-C, Co@N-C and N-C in O_2-saturated 0.1 M KOH solution. (d) K-L plots of Co@Fe-N-C at potential from 0.4 to 0.7 V in 0.1 M KOH. (e) Tafel plots of above samples in 0.1 M KOH. (f) RDE LSV curves of above samples in O_2-saturated 0.1 M $HClO_4$ solution.

previously reported Fe- and Fe-Co bimetal-based non-precious metal catalysts (Table S5 in the ESI).

LSV curves were obtained at various rotation speeds from 400 to 2500 rpm to analyze the process of electron transfer in alkaline media, and the current density was observed to increase with the increasing rotational speed (Fig. S12 in the ESI). In addition, Koutecky-Levich (K-L) plots are obtained from the K-L formula, and the results are used for analyzing the reaction kinetics (Fig. 4d). The excellent linearity and parallelism obtained in the range of 0.4 to 0.7 V, indicates first-order reaction kinetics for Co@Fe-N-C. In addition, Co@Fe-N-C exhibits the lowest Tafel slope (80.26 mV dec^{-1}) compared to Pt/C (93.67 mV dec^{-1}) compared to the catalysts with no CoNP present (95.05, 129.74, 140.06 and 88.76 mV dec^{-1} for Fe-N-C, Co@N-C, N-C and Co@Fe-N-C-A, respectively), confirming their

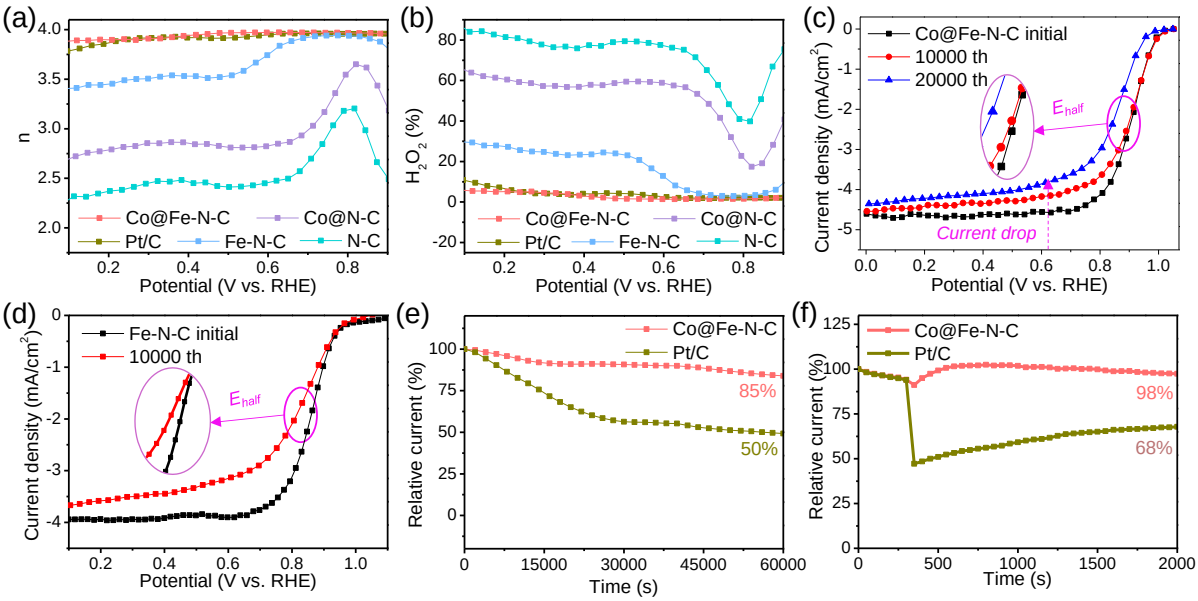

Figure 5. Electrocatalytic performance tests. (a) Electron transfer number (n), (b) yield of H_2O_2 (H_2O_2 %) of Pt/C, Co@Fe-N-C, Fe-N-C, Co@N-C and N-C. The stability test of (c) Co@Fe-N-C and (d) Fe-N-C before and after CV cycles. (e) long-term durability tests and (f) methanol tolerance testing of Co@Fe-N-C and Pt/C. The electrolyte for above testes is 0.1 M KOH solution and the rotating speed of RDE is 1600 rpm.

superior catalytic activity (Fig. 4e and Fig. S11b in the ESI). Moreover, the ORR activity of Co@Fe-N-C was tested in a O_2-saturated 0.1 M $HClO_4$ electrolyte. The LSV curves provide an $E_{1/2}$ = 0.79 V for Co@Fe-N-C, which is comparable to that of the Pt/C catalyst (0.82 V) and higher than those of Fe-N-C, Co@N-C and N-C samples (Fig. 4f). Tafel curves in acidic electrolyte are also investigated and the results indicates the Co@Fe-N-C has the lowest Tafel slope which corresponds to the superior activity (Fig. S13a in the ESI).

The number of transferred electrons, n, is another important parameter associated with the ORR catalysts. Based on the RRDE results, Co@Fe-N-C has the highest value of n = ~3.95 when compared with n = ~3.90 for Pt/C, n = ~3.70 for Fe-N-C, n = ~3.05 for Co@N-C, and n = ~2.75 for N-C in 0.1 M KOH (Fig. 5a). During the ORR process, hydrogen peroxide (H_2O_2) is produced as an intermediate product and can lead to catalyst poisoning, resulting in catalytic performance degradation. The yield of H_2O_2 from the RRDE results were tested and Co@Fe-N-C showed the lowest H_2O_2 yield of ~3%, while higher H_2O_2 quantities were detected in Pt/C (~5%), Fe-N-C (~15%), Co@N-C (~55%) and N-C (~72%) (Fig. 5b). Thus, the Co@Fe-N-C catalyst follows a direct four-electron reaction pathway, further confirming the excellent activity of this catalyst toward ORR in alkaline electrolyte. Stability of catalysts is crucial for their practical application in fuel cells and metal-air batteries. The LSV curves of Co@Fe-N-C (Fig. 5c) reveal a decrease of 10 mV and 50 mV in $E_{1/2}$ before and after 10,000 and 20,000 CV cycles, respectively. However, the stability test of CoNPs-free Fe-N-C shows 50 mV drop in $E_{1/2}$ after only 5000 cycles (Fig. 5d). An excellent alkaline ORR stability for the Co@Fe-N-C catalyst compared to Fe-N-C can be ascribed to the higher graphitization degree, more graphitic-N contents, and the synergy between CoNPs and Fe species of Co@Fe-N-C.[40] We note that these catalysts have poor acidic stability (see Fig. S13b in the ESI), likely due to the damage of CoNPs induced by acidic environment. Moreover, the long-term durability tests for Co@Fe-N-C also indicates an excellent performance with only 15% decrease in current after 60,000 s which is much lower than that of Pt/C catalyst (50% decrease in current), as shown in Fig. 5e. The methanol tolerance ability of ORR catalysts is very important for applications in fuel cells, particularly in case of direct methanol fuel cells. Fig. 5f shows the current-time (i-t) chronoamperometric response results of RDE testing, in which no obvious change in relative current could be observed for Co@Fe-N-C after addition of 5 mL of a 3 M aqueous solution of methanol at 300 s. However, the relative current is observed to drastically decrease in case of the Pt/C catalyst after the addition of methanol. Furthermore, the relative current of Co@Fe-N-C is 98% after 2000 s, which is considerably higher than that of the Pt/C catalyst (68%). The TEM images of Co@Fe-N-C after the stability (10,000 cycles) and long-term durability tests indicate that morphology of the catalyst and presence of CoNPs is not changed, indicating high structural stability of this catalyst in alkaline media (Fig. S14 in the ESI). The outstanding stability, long-term durability and tolerance of methanol-containing environment are essential for the practical application of this Co@Fe-N-C catalyst.

DFT theoretical calculations

The establish the origin of the enhanced catalytic activity of and to evaluate the specific role of CoNPs, we performed DFT calculations and compared Co@Fe-N-C and Fe-N-C catalysts (Table S6). As there is a very low content of CoNPs in Co@Fe-N-C, one particle exists in the large carbon matrix and the only different between Co@Fe-N-C and Fe-N-C is the existence of CoNPs (Fig. S15). Herein, simplified local structures of Co@Fe-N-C and Fe-N-C (Fig. S16, Fig. S17 in the

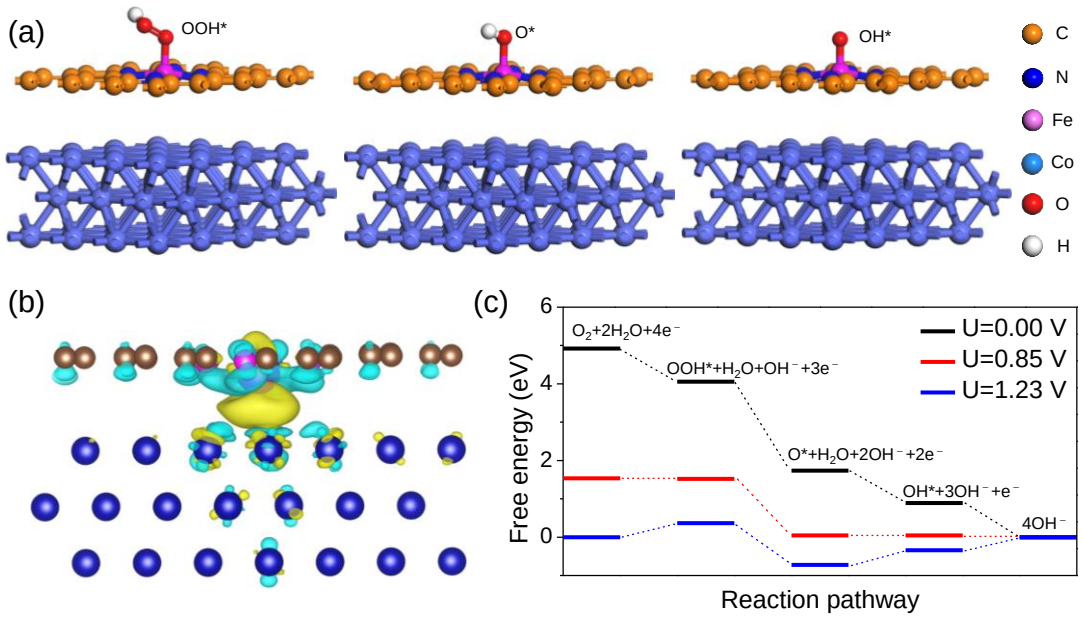

Figure 6. DFT calculation results. (a) Simplified structure charts of the intermediates OOH*, O*, and OH* for ORR on Co@Fe-N-C. (b) Calculated charge density difference of Co@Fe-N-C. (c) Free energy diagram of intermediates of Co@Fe-N-C from DFT calculation.

ESI) were considered. The comparatively large size of CoNPs can accommodate a number of Fe-N_4 active sites near a CoNP surface. Therefore, we examine the charge structure of the local structure of one Fe-N_4 in Fe-N_4-C in the presence of a CoNP. Fig. 6a shows that the three intermediates (OOH*, O*, and OH*) are adsorbed on the Fe-N_4 active center. The difference in charge density (Fig. 6b, Fig. S18 in the ESI) reflects the charge transfers from a CoNP to the Fe-N_4 active center, forming an electron-rich active site, which is beneficial for the ORR activity.

Furthermore, the performance of Co@Fe-N-C was evaluated based on the free energy diagram of ORR at its overpotential. A reduction in free energy could be observed at a potential of less than 0.85 V, indicating that the over potential of Co@Fe-N-C is 0.38 V (Fig. 6c). In contrast, the overpotential of Fe-N-C is 0.64 V (Fig. S19 in the ESI). The much lower overpotential of Co@Fe-N-C compared to those of Fe-N-C and commercial Pt/C (overpotential of 0.45 V).[51] theoretically confirms its superior ORR catalytic activity. This result is in good agreement with those obtained via the electrochemical performance tests. The energy diagram indicates that the density of states (DOS) near the Fermi level became sharper after CoNPs were introduced into Fe-N_4-C, indicating a considerable increase in conductivity of Co@Fe-N-C (Fig. S20 in the ESI) that is well agreement with Raman spectra results (i.e., high graphitization degree).

As discussed above, with the incorporation of CoNPs on the surface of Fe-N_4-C nanomaterials, Co@Fe-N-C performs lower overpotential, higher conductivity and more beneficial surface charge distribution, which are all crucial for the enhancement of ORR catalytic performance. Thus, the improved ORR performance of this Co@Fe-N-C catalyst can be partially attributed to the enhanced synergy between CoNPs and Fe-N_4 active sites and their positive effects on electron transfer.

Distribution of Co nanoparticles

To examine the effect of the distribution of CoNPs on the ORR activity, we produced Co@Fe-N-C using different experimental conditions, which affect the NP formation, including the pyrolysis temperature, Ar flow rate and Co contents.[52]

We investigated the effect of Co content on the distribution of CoNPs and ORR activity of the catalyst with $m_{Co\text{-}ZIF}$ = 50, 100, 200, 300 mg per $m_{Fe\text{-}ZIF\text{-}8}$ = 100 mg. We found that the density of CoNPs increased from 0.04 wt.% to 0.14 wt.% and the higher density of CoNPs generally corresponded to higher ORR activity (Fig. S21, S22 and Table S7 in the ESI).

We also explored the effect of heat treatment temperature on formation of CoNPs and the ORR activity of Co@Fe-N-C. We further found that the density of formed CoNPs and their location is strongly affected by the treatment temperature and the greater ORR activity was observed for catalysts with higher CoNPs density. For example, the sample treated at T = 700 °C (Co content, 0.04 wt.%) reveals some isolated CoNPs out of the surface of Fe-N_4-C nanomaterials and has poor performance with $E_{1/2}$=0.67 V, while the samples treated at T = 800 °C (Co content, 0.06 wt.%) and T=1000 °C (Co content 0.06 wt.%) have higher $E_{1/2}$=0.82 V and 0.84 V, respectively. The sample treated at T=900°C (the largest Co content 0.10 wt.%) shows the highest CoNPs density and best performance with $E_{1/2}$=0.92 V (Fig. S23, S24, S25 and Table S7 in the ESI).

We also found that Ar flow rates (10 mL/min, 50 mL/min, 100 mL/min) greatly affect the formation of CoNPs. The highest density of CoNPs was observed for Ar flow rate of 50 mL/min. The ORR activity was affected by the flow rate: $E_{1/2}$=0.86 V (Co content 0.04 wt.%, Ar rate - 10 mL/min), $E_{1/2}$=0.92 V (Co content 0.10 wt.%, Ar rate - 50 mL/min) and $E_{1/2}$=0.82 V (Co content 0.01 wt.%, Ar rate - 100 mL/min), revealing clear link between the higher CoNP density and better ORR activity (Fig. S26, S27 and Table S7 in the ESI).

We also examined the effect of the sizes of CoNPs in Co@Fe-N-C on the ORR activity and found that smaller CoNPs sizes do not refer to better ORR performance. Instead, the higher CoNPs density and more uniform distribution of CoNPs on Co@Fe-N-C have significant effect on the ORR performance (Table S8 in the ESI). Overall, we attribute enhanced ORR performance of to the Co@Fe-N-C s due to the combination of the factors, such as CoNP induced decrease of the overpotential of Fe-N4 sites, increase of specific surface area and a larger number of graphitic-N.

Conclusions

In summary, we successfully prepared the Co@Fe-N-C catalyst containing CoNPs loaded on the surface of Fe-N_4-C nanomaterials using an assisted thermal loading method. This catalyst exhibited an excellent ORR activity with 20 mV higher $E_{1/2}$ than Pt/C in 0.1 M KOH solution and a considerable activity with only 30 mV lower $E_{1/2}$ than Pt/C in 0.1 M $HClO_4$ electrolyte. Moreover, this catalyst exhibits an expected 4-electron pathway, low yield of H_2O_2 (lower than 3%), outstanding stability with negligible decrease in $E_{1/2}$ after 10,000 cycles, remarkable methanol tolerance and long-term durability (85% in current after 60,000 s) in alkaline electrolyte. Microscopic characterizations indicated that Co@Fe-N-C had larger specific surface area and higher graphitic-N content compared to Fe-N-C. Density functional theory calculations further supported the positive effect of CoNP and suggested the enhanced synergy between CoNPs and Fe-N_4 sites. Thus, the incorporation of CoNPs into the Fe-N-C catalyst led to enhancement of the ORR activity. This study provides a new route to prepare practical, high-performance, and low-cost ORR catalysts, which will promote their application in devices such as fuel cells and metal-air batteries.

Author Contributions

TJ developed methodology and performed experimental studies. WL conceptualized the study and provided supervisions. TJ, WL and LT analysed the data and co-wrote the manuscript. QF provided resources for the study. All authors approved manuscript submission.

Conflicts of interest

There are no conflicts to declare.

Acknowledgements

This work is financially supported by SAIC Group Co., Ltd., Passenger Vehicle Company, Department of Prospective Technology and Shanghai Automobile Industry Science and Technology Development Foundation (1801).

References

1 L. Xue, Y. Li, X. Liu, Q. Liu, J. Shang, H. Duan, L. Dai and J. Shui, *Nat. Commun.*, 2018, **9**, 3819.
2 U. Martinez, S. Komini Babu, E. F. Holby, H. T. Chung, X. Yin and P. Zelenay, *Adv. Mater.*, 2019, **31**, 1806545.
3 M. Luo, Z. Zhao, Y. Zhang, Y. Sun, Y. Xing, F. Lv, Y. Yang, X. Zhang, S. Hwang, Y. Qin, J. Y. Ma, F. Lin, D. Su, G. Lu and S. Guo, *Nature*, 2019, **574**, 81–85.
4 L. Chen, X. Xu, W. Yang and J. Jia, *Chinese Chem. Lett.*, 2020, **31**, 626–634.
5 B. K. Barman, B. Sarkar, P. Ghosh, M. Ghosh, G. M. Rao and K. K. Nanda, *ACS App. Energy Mater.*, 2019, **2**, 7330–7339.
6 W. Kiciński, J. P. Sęk, E. Matysiak-Brynda, K. Miecznikowski, M. Donten, B. Budner and A. M. Nowicka, *Appl. Catal. Environ.*, 2019, **258**, 117955.
7 C. Lo Vecchio, A. S. Aricò, G. Monforte and V. Baglio, *Renew. Energy*, 2018, **120**, 342–349.
8 X. Liu, H. Liu, C. Chen, L. Zou, Y. Li, Q. Zhang, B. Yang, Z. Zou and H. Yang, *Nano Res.*, 2019, **12**, 1651–1657.
9 Y. Liu, X. Wang, B. Zhao, X. Shao and M. Huang, *Chem. Eur. J.*, 2019, **25**, 9650–9657.
10 A. Song, L. Cao, W. Yang, Y. Li, X. Qin and G. Shao, *ACS Sustain. Chem. Eng.*, 2018, **6**, 4890–4898.
11 X. Peng, T. J. Omasta, E. Magliocca, L. Wang, J. R. Varcoe and W. E. Mustain, *Angew. Chem. Int. Ed.*, 2019, **58**, 1046–1051.
12 H. Wu, W. Sun, J. Shen, D. W. Rooney, Z. Wang and K. Sun, *Nanoscale*, 2018, **10**, 10221–10231.
13 D. Lyu, Y. Du, S. Huang, B. Y. Mollamahale, X. Zhang, S. W. Hasan, F. Yu, S. Wang, Z. Q. Tian and P. K. Shen, *ACS Appl. Mater. Inter.*, 2019, **11**, 39809–39819.
14 E. Luo, H. Zhang, X. Wang, L. Gao, L. Gong, T. Zhao, Z. Jin, J. Ge, Z. Jiang, C. Liu and W. Xing, *Angew. Chem. Int. Ed.*, 2019, **58**, 12469–12475.
15 J. Li, M. Chen, D. A. Cullen, S. Hwang, M. Wang, B. Li, K. Liu, S. Karakalos, M. Lucero, H. Zhang, C. Lei, H. Xu, G. E. Sterbinsky, Z. Feng, D. Su, K. L. More, G. Wang, Z. Wang and G. Wu, *Nat. Catal.*, 2018, **1**, 935–945.
16 M. E. Kreider, A. Gallo, S. Back, Y. Liu, S. Siahrostami, D. Nordlund, R. Sinclair, J. K. Nørskov, L. A. King and T. F. Jaramillo, *ACS Appl. Mater. Inter.*, 2019, **11**, 26863–26871.
17 N. Zhang, L. Cao, L. Feng, J. Huang, K. Kajiyoshi, C. Li, Q. Liu, D. Yang and J. He, *Nanoscale*, 2019, **11**, 11542–11549.
18 Y. Li, T. Liu, W. Yang, Z. Zhu, Y. Zhai, W. Gu and C. Zhu, *Nanoscale*, 2019, **11**, 19506–19511.
19 G. A. Ferrero, K. Preuss, A. Marinovic, A. B. Jorge, N. Mansor, D. J. L. Brett, A. B. Fuertes, M. Sevilla and M. M. Titirici, *ACS Nano*, 2016, **10**, 5922–5932.
20 J. Guo, Y. Cheng and Z. Xiang, *ACS Sustain. Chem. Eng.* 2017, **5**, 7871–7877.
21 M. Karuppannan, J. E. Park, H. E. Bae, Y. H. Cho and O. J. Kwon, *Nanoscale*, 2020, **12**, 2542–2554.
22 X. Sun, P. Wei, S. Gu, J. Zhang, Z. Jiang, J. Wan, Z. Chen, L. Huang, Y. Xu, C. Fang, Q. Li, J. Han and Y. Huang, *Small*, 2020, **16**, 1906057.
23 T. Varga, G. Ballai, L. Vásárhelyi, H. Haspel, Á. Kukovecz and Z. Kónya, *Appl. Catal. Environ.*, 2018, **237**, 826–834.
24 Q. Ke, L. Yang, Y. Gao, X. L. Wu, F. Chen, S. Liu, H. Lin, C. Z. Yuan and J. Chen, *Nanotechnology*, 2020, **31**, 165401.
25 X. Chen, D. D. Ma, B. Chen, K. Zhang, R. Zou, X. T. Wu and Q. L. Zhu, *Appl. Catal. Environ.*, 2020, **267**, 118720.
26 Y. Wang, X. Yin, H. Shen, H. Jiang, J. Yu, Y. Zhang, D. Li, W. Li and J. Li, *Inter. J. Hydrogen Energy*, 2018, **43**, 20687–20695.
27 X. Zhang, Y. B. Mollamahale, D. Lyu, L. Liang, F. Yu, M. Qing, Y. Du, X. Zhang, Z. Q. Tian and P. K. Shen, *J. Catal.*, 2019, **372**, 245–257.
28 F. Xiao, G. L. Xu, C. J. Sun, M. Xu, W. Wen, Q. Wang, M. Gu, S. Zhu, Y. Li, Z. Wei, X. Pan, J. Wang, K. Amine and M. Shao, *Nano Energy*, 2019, **61**, 60–68.
29 L. Chai, Q. Huang, H. Cheng, X. Wang, L. Zhang, T. T. Li, Y. Hu, J. Qian and S. Huang, *Nanoscale*, 2020, **12**, 8785–8792.
30 W. Xie, Z. Li, S. Jiang, J. Li, M. Shao and M. Wei, *Chem. Eng. J.*, 2019, **373**, 734–743.
31 X. Chen, K. Shen, J. Chen, B. Huang, D. Ding, L. Zhang and Y. Li, *Chem. Eng. J.*, 2017, **330**, 736–745.
32 W. L. Xin, K. K. Lu and D. Shan, *Appl. Surf. Sci.*, 2019, **481**, 313–318.
33 H. Jin, H. Zhou, W. Li, Z. Wang, J. Yang, Y. Xiong, D. He, L. Chen and S. Mu, *J. Mater. Chem. A*, 2018, **6**, 20093–20099.
34 W. Xue, Q. Zhou, F. Li and B. S. Ondon, *J. Power Sources*, 2019, **423**, 9–17.
35 L. Gao, M. Xiao, Z. Jin, C. Liu, J. Zhu, J. Ge and W. Xing, *J. Energy Chem.*, 2018, **27**, 1668–1673.
36 H. Tan, J. Tang, J. Henzie, Y. Li, X. Xu, T. Chen, Z. Wang, J. Wang, Y. Ide, Y. Bando and Y. Yamauchi, *ACS Nano*, 2018, **12**, 5674–5683.
37 C. Wang, W. Chen, K. Xia, N. Xie, H. Wang and Y. Zhang, *Small*, 2019, **15**, 1804966.
38 C. Li, Z. Yu, H. Liu and M. Xiong, *Chem. Eng. J.*, 2019, **371**, 433–442.
39 M. Wang, H. Zhang, G. Thirunavukkarasu, I. Salam, J. R. Varcoe, P. Mardle, X. Li, S. Mu and S. Du, *ACS Energy Lett.*, 2019, **4**, 2104–2110.
40 J. Wang, Z. Huang, W. Liu, C. Chang, H. Tang, Z. Li, W. Chen, C. Jia, T. Yao, S. Wei, Y. Wu and Y. Li, *J. Am. Chem. Soc.*, 2017, **139**, 17281–17284.
41 J. Li, Y. Kang, W. Wei, X. Li, Z. Lei and P. Liu, *Chem. Eng. J.*, 2021, **407**, 127961.
42 L. Chen, Y. Zhang, L. Dong, W. Yang, X. Liu, L. Long, C. Liu, S. Dong and J. Jia, *J. Mater. Chem. A*, 2020, **8**, 4369–4375.
43 M. Xiao, J. Zhu, L. Ma, Z. Jin, J. Ge, X. Deng, Y. Hou, Q. He, J. Li, Q. Jia, S. Mukerjee, R. Yang, Z. Jiang, D. Su, C. Liu and W. Xing, *ACS Catal.*, 2018, **8**, 2824–2832.
44 J. C. Li, S. Maurya, Y. S. Kim, T. Li, L. Wang, Q. Shi, D. Liu, S. Feng, Y. Lin and M. Shao, *ACS Catal.*, 2020, **10**, 2452–2458.
45 J. Luo, K. Wang, X. Hua, W. Wang, J. Li, S. Zhang and S. Chen, *Small*, 2019, **15**, 1805325.
46 Z. S. Wu, L. Chen, J. Liu, K. Parvez, H. Liang, J. Shu, H. Sachdev, R. Graf, X. Feng and K. Müllen, *Adv. Mater.*, 2014, **26**, 1450–1455.
47 C. Hu, C. Yu, M. Li, X. Wang, Q. Dong, G. Wang and J. Qiu, *Chem. Commun.*, 2015, **51**, 3419–3422.
48 A. Zitolo, V. Goellner, V. Armel, M. T. Sougrati, T. Mineva, L. Stievano, E. Fonda and F. Jaouen, *Nat. Mater.*, 2015, **14**, 937–942.
49 K. Strickland, E. Miner, Q. Jia, U. Tylus, N. Ramaswamy, W. Liang, M. T. Sougrati, F. Jaouen and S. Mukerjee, *Nat. Commun.*, 2015, **6**, 7343.
50 D. Xia, X. Yang, L. Xie, Y. Wei, W. Jiang, M. Dou, X. Li, J. Li, L. Gan and F. Kang, *Adv. Funct. Mater.*, 2019, **29**, 1906174.
51 J. K. Nørskov, J. Rossmeisl, A. Logadottir, L. Lindqvist, J. R. Kitchin, T. Bligaard and H. Jónsson, *J. Phys. Chem. B*, 2004, **108**, 17886–17892.
52 T. Jiang, W. Luan, Y. Ren, C. Fan, Q. Feng and L. Turyanska, *Micropor. Mesopor. Mater.*, 2020, **305**, 110382.